The Astrophysical Journal, 876:52 (13pp), 2019 May 1 https://doi.org/10.3847/1538-4357/ab1010

Alignment between Filaments and Galaxy Spins from the MaNGA Integral-field Survey

Alex Krolewski[1,2], Shirley Ho[2,3,4,5], Yen-Chi Chen[6], P. F. Chan[2,7], Ananth Tenneti[3], Dmitry Bizyaev[8,9], and Katarina Kraljic[10]

[1] Department of Astronomy, University of California at Berkeley, New Campbell Hall, Berkeley, CA 94720, USA; krolewski@berkeley.edu
[2] Lawrence Berkeley National Lab, 1 Cyclotron Road, Berkeley, CA 94720, USA
[3] Department of Physics, Carnegie Mellon University, Pittsburgh, PA 15213, USA
[4] McWilliams Center for Cosmology, Carnegie Mellon University, Pittsburgh, PA 15213, USA
[5] Berkeley Center for Cosmological Physics, University of California at Berkeley, New Campbell Hall, Berkeley, CA 94720, USA
[6] Department of Statistics, University of Washington, Seattle, WA 98105, USA
[7] The Chinese University of Hong Kong, Shatin, NT, Hong Kong SAR, People's Republic of China
[8] Apache Point Observatory and New Mexico State University, P.O. Box 59, Sunspot, NM 88349-0059, USA
[9] Sternberg Astronomical Institute, Moscow State University, Moscow, Russia
[10] Institute for Astronomy, University of Edinburgh, Royal Observatory, Blackford Hill, Edinburgh, EH9 3HJ, UK

Received 2018 August 7; revised 2019 February 26; accepted 2019 March 13; published 2019 May 1

Abstract

Halos and galaxies acquire their angular momentum during the collapse of the surrounding large-scale structure. This process imprints alignments between galaxy spins and nearby filaments and sheets. Low-mass halos grow by accretion onto filaments, aligning their spins with the filaments, whereas high-mass halos grow by mergers along filaments, generating spins perpendicular to the filament. We search for this alignment signal using filaments identified with the "Cosmic Web Reconstruction" algorithm applied to the Sloan Digital Sky Survey Main Galaxy Sample and galaxy spins from the Mapping Nearby Galaxies at Apache Point Observatory (MaNGA) integral-field unit survey. MaNGA produces a map of the galaxy's rotational velocity, allowing direct measurement of the galaxy's spin direction, or unit angular momentum vector projected onto the sky. We find no evidence for alignment between galaxy spins and filament directions. We do find hints of a mass-dependent alignment signal, which is in 2σ–3σ tension with the mass-dependent alignment signal in the MassiveBlack-II and Illustris hydrodynamical simulations. However, the tension vanishes when galaxy spin is measured using the Hα emission line velocity rather than stellar velocity. Finally, in simulations we find that the mass-dependent transition from aligned to anti-aligned dark matter halo spins is not necessarily present in stellar spins: we find a stellar spin transition in Illustris but not in MassiveBlack-II, highlighting the sensitivity of spin-filament alignments to feedback prescriptions and subgrid physics.

Key words: cosmology: observations – galaxies: evolution – galaxies: formation – large-scale structure of universe

1. Introduction

Dark matter protohalos acquire their angular momentum through tidal torquing by neighboring large-scale structure (Peebles 1969; Doroshkevich 1970; White 1984). In the linear regime, angular momentum grows linearly with time and is aligned along the intermediate eigenvector of the tidal tensor (i.e., the traceless part of the Hessian of the potential Φ). However, tidal torque theory is only qualitatively correct in the nonlinear regime, as nonlinear evolution significantly weakens the spin alignment (Porciani et al. 2002) and drives alignments with other preferred directions. In the Zel'dovich picture of structure formation, collapse occurs sequentially along the eigenvectors of the tidal tensor (Zel'dovich 1970), forming anisotropic structures such as sheets (one direction of collapse and two of expansion) and filaments (two directions of collapse and one of expansion). Halos in filaments therefore acquire spin parallel to the filament, as matter collapses and rotates in the plane perpendicular to the filament (Pichon et al. 2011; Codis et al. 2012). N-body and hydrodynamic simulations have confirmed this result for low-mass halos ($M \lesssim 10^{12}\,M_\odot$), while finding that mergers align high-mass halo spins perpendicular to filaments by converting motion along the filament into spin (Bailin & Steinmetz 2005; Aragón-Calvo et al. 2007b; Hahn et al. 2007; Codis et al. 2012, 2015; Trowland et al. 2013; Aragon-Calvo & Yang 2014; Dubois et al. 2014; Ganeshaiah Veena et al. 2018; Wang et al. 2018; Wang & Kang 2018).

Observations probe the spin of baryons within the galaxy rather than the spin of dark matter in the host halo. Initially, the baryons and dark matter share the same angular momentum distribution and the baryons conserve angular momentum as they collapse, creating a rotation-supported disk (Fall & Efstathiou 1980; Blumenthal et al. 1986; Mo et al. 1998). The size and profile of the baryonic disk, as computed from the angular momentum profile and dimensionless spin λ of halos in N-body simulations, are roughly consistent with observations (Fall 1983; Bullock et al. 2001). This simple picture cannot be correct in detail, however, because the baryons are subject to different physical processes than the dark matter, including dissipation, disk instabilities, and feedback-driven outflows (Danovich et al. 2015). These processes lead to misalignments between the spins of the dark matter and the baryons (van den Bosch et al. 2002; Bett 2012). As a result, the mass-dependent alignment transition found in simulations, which typically use gravity-only N-body codes (but see Dubois et al. (2014) and Codis et al. (2015) for spin-filament alignments in hydrodynamic simulations), may not be present in observations or hydrodynamic simulations of galaxy alignments.

Alignments between galaxy spins and large-scale structure have been measured using imaging to infer the galaxy's inclination and spin axis from its axis ratio and position angle. At $z \sim 0$, studies have found suggestive but ultimately not significant evidence for correlations between the chirality of neighboring galaxy spins (Slosar et al. 2009; Andrae & Jahnke 2011; Lee 2011). Studies of alignments between galaxy spins and large-scale structure have reached conflicting conclusions. Early studies from small galaxy samples in photographic plate surveys yielded weak and conflicting results (Gregory et al 1981; Dekel 1985; Cabanela & Aldering 1998 and references therein). More recent results from larger samples suggested that spiral galaxies are aligned along the intermediate axis of the tidal tensor, in accord with predictions from tidal torque theory (Lee & Pen 2002; Lee & Erdogdu 2007), and are therefore aligned perpendicular to filaments (Jones et al. 2010; Zhang et al. 2015). However, a number of studies within the past few years have found little support for tidal torque theory predictions and instead suggest that low-mass spiral spins are parallel to filaments, while higher-mass elliptical or lenticular spins are perpendicular to filaments (Tempel et al. 2013; Tempel & Libeskind 2013; Pahwa et al. 2016).

Alignments between galaxy spins are of particular interest, as they are a major source of systematic error for weak lensing shear measurements, particularly for upcoming missions such as LSST (LSST Science Collaboration et al. 2009), WFIRST (Spergel et al. 2015), and EUCLID (Laureijs et al. 2011) that aim to measure the dark energy equation of state (Bridle & King 2007; Kirk et al. 2012). For disk galaxies, galaxy ellipticities arise from galaxy spins and are quadratic in the tidal field under tidal torque theory (Lee & Pen 2000; Catelan et al. 2001), while for elliptical galaxies, ellipticity arises directly from stretching by tidal fields and is linearly related to the tidal field (Hirata & Seljak 2004). As a result, measurements of alignments between galaxy spins and the surrounding tidal field or large-scale structures (clusters, filaments, sheets, and voids) can inform physical models of intrinsic alignments, particularly for disk galaxies, whose intrinsic alignment remains poorly constrained (Hirata et al. 2007; Mandelbaum et al. 2011).

We measure spin-filament alignments using galaxy spins determined from integral-field kinematics rather than from galaxy imaging. Our method is complementary to imaging-based spin measurements, as it has very different sources of systematic error. Galaxies often have low-surface brightness features such as spiral arms or tidal tails; therefore, the galaxy shape may depend strongly on the measurement method, e.g., which isophote is used (see Figure 1 in Kirk et al. 2015). Similarly, galactic bulges can bias shape measurements even for very late-type galaxies (Andrae & Jahnke 2011). While careful modeling including bulge/disk decomposition can alleviate this bias (e.g., Tempel et al. 2013; Tempel & Libeskind 2013), using kinematics to measure galaxy spin eliminates the need for complex models of galaxy morphology and their associated uncertainty.

In this paper, we measure the alignment between filaments identified in the SDSS Main Galaxy Sample and galaxy spins measured from Mapping Nearby Galaxies at Apache Point Observatory (MaNGA) kinematics. We use the filament catalog of Chen et al. (2016), which finds filaments as ridges in the density field using the subspace-constrained mean-shift algorithm (Section 2). We find no preference for spin-filament alignments in our overall sample of ∼2700 galaxies, and we validate our results by finding similar alignments between galaxies and the Bisous model filaments of Tempel et al. (2014) (Section 3). We compare our results to spin-filament alignments in hydrodynamical simulations by measuring the mass dependence of the alignment signal, and find 2σ–3σ tension when using spins measured from the stellar continuum, but no tension when using spins measured from the Hα emission line (Section 4). Finally, we compare our results to previous findings and conclude in Section 5.

In this paper we use a flat ΛCDM cosmology with $\Omega_m = 0.3$ and $h = 0.7$. We convert all masses to $M_\odot$ for an intercomparison between observations and simulations.

2. Methods and Data

2.1. Filament Finder

A variety of methods have been used to find filaments in observations and simulations, including approaches identifying filaments as eigenvectors of the deformation tensor (Hahn et al. 2007; Jasche et al. 2010), velocity shear tensor (Libeskind et al. 2013), or Hessian of the density field (Aragón-Calvo et al. 2007b); identification of filaments as ridges in the density field (Sousbie et al. 2008; Chen et al. 2015); and searches for cylindrical arrangements of galaxies (Tempel et al. 2014). For a comprehensive overview, see Cautun et al. (2014).

We use the publicly available Cosmic Web Reconstruction filament algorithm[11] (Chen et al. 2016) to identify filaments in the SDSS Main Galaxy Sample. This filament finder identifies filaments as curves in 2D (α, δ) slices of width $\delta z = 0.005 \sim 20$ Mpc. This yields a well-defined orientation for every point on the filament and makes it easy to cross-correlate with the spin of nearby galaxies. The filament finder is explained in detail in Chen et al. (2015), so we only provide a brief description here. Our filament catalog differs slightly from the publicly available catalog of Chen et al. (2015), as it extends to lower redshift and uses slightly different thresholding to remove noisy filaments.

The filament finder operates on a smoothed density field created from the positions of galaxies in the SDSS Main Galaxy Sample (Blanton et al. 2005) and the LOWZ and CMASS samples from BOSS (Alam et al. 2015), with a redshift-dependent Gaussian smoothing kernel that ranges between 5 and 10 Mpc (Figure 6 in Chen et al. 2016). It identifies filaments as density ridges of the smoothed density field, or local maxima along the second eigenvector of the Hessian of the density field.

The filament finder uses 2D slices of width $\delta z = 0.05$ ($c\delta z = 1500$ km s^{-1} ~ 20 Mpc); in each slice, it finds filaments in an equirectangular projection of equatorial coordinates (α, δ) using only galaxies in the North Galactic Cap (Figure 1). We find filaments between $z = 0.02$ and $z = 0.15$, with the lower limit set by the sparsity of SDSS galaxies at $z < 0.02$ and the upper limit set by the maximum redshift of MaNGA galaxies ($z = 0.15$). At these redshifts the filament finder primarily uses galaxies from the Main Galaxy Sample. We eliminate galaxies in the 10% least dense environments, defined using the distance to the 30th-nearest neighbor. This eliminates noisy filaments from very low-density regions without removing too many filaments. Varying the thresholding criteria does not qualitatively change the results in Table 1.

We define the filament orientation at each point as the first principal component of the covariance matrix of the positions of the 10 nearest neighbor points. We estimate the uncertainty on the filament directions at each point by measuring the local filament orientation for 100 bootstrap resamples of the filament catalog.

---

[11] https://sites.google.com/site/yenchicr/

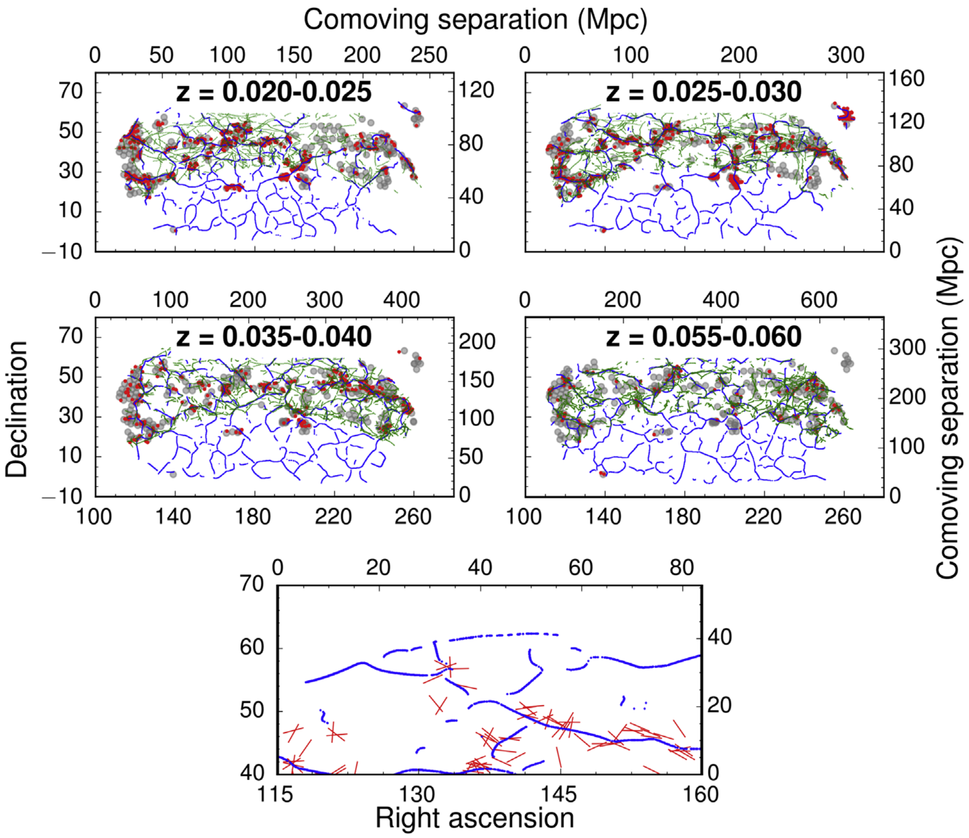

Figure 1. Upper four panels: MaNGA galaxies (red) located within 40 Mpc of Cosmic Web Reconstruction filaments (blue) and Tempel et al. (2014) Bisous filaments (green). Slices were chosen as the lowest-redshift slice with filaments ($z = 0.02$) and the three quartiles of the MaNGA galaxy redshift distribution ($z = 0.027$, 0.036, and 0.052). The gray circles indicate MaNGA plates released with MPL-6. Lower panel: comparison between galaxy spins (red lines) and Cosmic Web Reconstruction filaments (blue lines) for a section of the sky at $z = 0.025$–0.03.

Filaments are identified in two dimensions rather than three for ease of interpretation: collapsing along the line of sight eliminates spurious filaments created by redshift-space distortions and allows us to better model the strong redshift dependence of galaxy density, which requires a redshift-dependent smoothing length (Chen et al. 2016). Furthermore, previous work measuring 3D spin-filament alignments has found that line-of-sight biases in both galaxy spins and filaments creates strong spurious alignment signals that must be corrected (Tempel et al. 2013; Tempel & Libeskind 2013). From simulations, we expect that using 2D rather than 3D filaments reduces our signal by ∼40% (Appendix B); thus we believe the moderate loss in signal is worth the substantial reduction in systematic errors.

In Figure 1 we plot the MaNGA galaxy sample (with $z > 0.02$ and distance to filament $d_F < 40$ Mpc) and the Cosmic Web Reconstruction filaments in four redshift slices: $z = 0.02$–0.025, the lowest-redshift slice, and the slices containing the three quartiles of the redshift distribution, $z = 0.025$–0.03, 0.035–0.04, and 0.055–0.06. In Figure 1, most galaxies are clearly closest to a single filament, indicating that confusion between filaments will not contribute significantly to noise in the measurement.

To check our results, we measure alignments with the Tempel et al. (2014) filament catalog,[12] which is also derived from galaxies in the SDSS Main Galaxy Sample, with $0.009 < z < 0.155$. Tempel et al. (2014) is a very different method from Chen et al. (2015): they find filaments using the Bisous model, a marked point process model that fits the galaxy data to a filamentary network composed of connected cylinders of fixed width. They find filaments in three dimensions, suppressing peculiar velocities by estimating the velocity dispersions for galaxy groups. We measure alignments using galaxies within 20 h^{-1} Mpc of filaments and with a velocity-corrected distance from the Tempel et al. (2014) catalog, yielding a sample of 3028 galaxies. For each galaxy, we consider its alignment with the plane-of-sky projection of the nearest Tempel et al. (2014) filament. We compare the Tempel et al. (2014) and Chen et al. (2015) filaments in Figure 1; Tempel et al. (2014) identify significantly smaller-scale filaments, but on larger scales both methods recover similar filaments. Despite the substantial methodological differences between the two filament finders, we find largely similar alignments (Section 3).

2.2. MaNGA Galaxies

MaNGA is an integral-field survey that aims to obtain spectra of 10,000 nearby galaxies (Bundy et al. 2015). It began in 2014 July as part of SDSS-IV (Blanton et al. 2017) and is planned to continue until 2020. MaNGA uses the 2.5 m SDSS telescope at Apache Point Observatory in New Mexico (Gunn et al. 2006) and the dual fiber-fed BOSS spectrographs (Smee et al. 2013), but rather than allocating a single fiber per galaxy like previous SDSS surveys, each plate contains 17 pluggable

---

[12] Available on Vizier, http://vizier.cfa.harvard.edu/viz-bin/VizieR?-source=J/MNRAS/438/3465, including a filament catalog; catalog of filament points; and catalog of all galaxies used to construct the filament catalog and their velocity corrected distances.

Table 1
Cosmic Web Reconstruction Alignments for Different Subsamples

Sample	N	$\langle \cos\theta \rangle$	SE	Shuffle Mean	σ from Shuffle
All	2736	0.6452	0.0075	0.6406	0.61
$D_F < 0.6$ Mpc	684	0.6474	0.0144	0.6438	0.25
$0.6 < D_F < 1.4$ Mpc	684	0.6532	0.0148	0.6427	0.71
$1.4 < D_F < 3.0$ Mpc	684	0.6497	0.0146	0.6370	0.87
$D_F > 3.0$ Mpc	684	0.6257	0.0154	0.6365	−0.70
$M_\star < 10.02$	684	0.6601	0.013	0.6406	1.50
$10.02 < M_\star < 10.47$	684	0.6288	0.0120	0.6425	−1.14
$10.47 < M_\star < 10.87$	684	0.6350	0.0125	0.6407	−0.46
$M_\star > 10.87$	684	0.6500	0.0147	0.6358	0.97
$u - r < 1.70$	684	0.6562	0.0139	0.6417	1.04
$1.70 < u - r < 2.09$	684	0.6381	0.0149	0.6409	−0.19
$2.09 < u - r < 2.35$	684	0.6630	0.0130	0.6354	2.12
$u - r > 2.35$	684	0.6072	0.0168	0.6373	−1.79
elliptical	1039	0.6408	0.0130	0.6392	0.12
spiral	676	0.6423	0.0147	0.6399	0.16
edge-on	344	0.6239	0.0186	0.6392	−0.82

Note. MaNGA spin-Cosmic Web Reconstruction filament alignments for the entire sample and subsamples split by distance to filament (D_F), stellar mass (in units of $\log M_\odot$), $u - r$ color, and morphology. $\langle \cos\theta \rangle$ is the mean dot product between the unit spin vector and the unit filament vector. SE is the standard error of the mean, calculated using 50,000 bootstrap resamples of the data. We measure the expectation for random alignments using 50,000 shuffles of the data, and compute σ, the deviation between the data and the randoms, in units of the standard error.

IFUs, each of which consists of hexagonal bundles containing between 19 and 127 fibers with a typical spatial resolution of 2″5 or 1.8 kpc at $z = 0.03$ (Drory et al. 2015). The dual spectrograph design enables a wavelength coverage of 3600–10000 Å with a velocity resolution of 70 km s^{-1} (Smee et al. 2013). Typical exposure times of 3 hr ensured a signal-to-noise ratio (S/N) of 5 at the outskirts of targeted galaxies, and much greater toward the center (Law et al. 2015). Spectrophotometric calibration is accurate to <5% (Yan et al. 2016b) and the data reduction pipeline is described in Law et al. (2016).

The MaNGA targeting sample consists of 10,000 galaxies with $0.01 < z < 0.15$ (median $z \sim 0.03$). The sample was chosen to have a flat number-density distribution in absolute i-band magnitude M_i while maximizing the spatial resolution and ensuring IFU coverage to a few times the half-light radius R_e (Yan et al. 2016a). As a result, stellar mass is highly correlated with redshift for the MaNGA sample, as galaxies of a given mass (and thus radius) are preferentially targeted at a redshift where the IFUs cover a few R_e (Figure 2). The double-peaked redshift-mass distribution is a result of the two-tiered MaNGA selection process, consisting of the Primary sample with coverage to $1.5R_e$ and the Secondary sample with coverage to $2.5R_e$. Galaxies are assigned to plates via a tiling algorithm that is unbiased with respect to environment, and to IFUs in a way that maximizes the number of galaxies covered to the appropriate radius (1.5 R_e for the Primary sample and 2.5 R_e for the Secondary sample).

We use the MPL-6 data release of MaNGA with v2_3_1 of the Data Reduction Pipeline and v2.1.3 of the Data Analysis Pipeline. MPL-6 contains 4687 galaxy data cubes observed between 2014 March and 2017 July, of which 70 are repeat observations. We subsequently reduce our sample to 2736 galaxies via a variety of quality cuts. We remove 85 galaxies with the CRITICAL DRP3QUAL maskbit set, which indicates a variety of problems ranging from unmasked cosmic rays to IFUs partially falling out of the plate; 426 galaxies targeted as part of ancillary programs, which lack well-defined selection weights; 393 galaxies with $z < 0.02$; and 478 galaxies lying beyond the 40 Mpc radius of influence for galaxy-filament alignments found in Chen et al. (2019). Finally, we remove galaxies with poorly measured spins (see Section 2.3): 19 galaxies lacking a sufficient number of points to fit a spin; 170 galaxies with multiple galaxies inside the IFU (Figure 4); and 858 galaxies with position angle error >5°, which we find by visual inspection to generally have poorly defined spins.

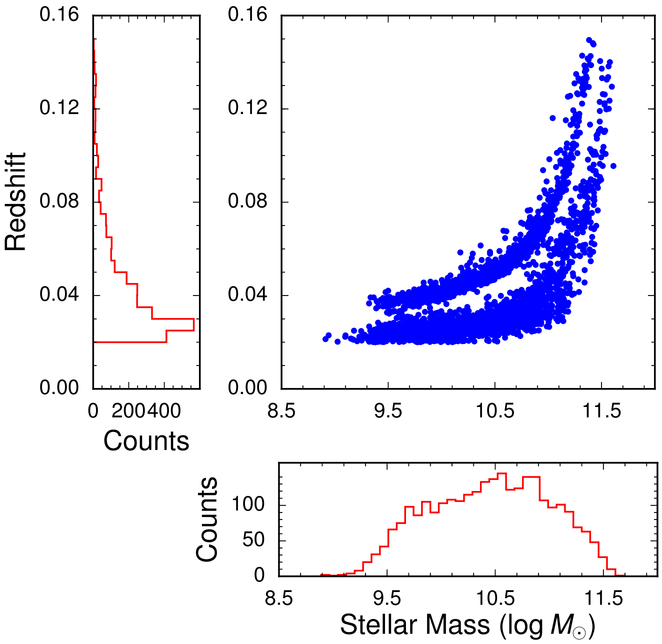

Figure 2. Redshift (top) and stellar mass (bottom) distributions of the MaNGA sample of 2736 galaxies (selected according to criteria in Section 2.3).

We weight each galaxy to create a volume-limited sample (Wake et al. 2017) that is appropriate to compare to simulations. Specifically, we weight each galaxy by the "esrweights" (Equation (A12) in Wake et al. 2017), the effective volume over which it could have been observed. The weights are necessary because MaNGA is not a volume-limited sample; the flat distribution in M_i leads to to biases toward higher luminosity at fixed mass, biasing galaxy colors and inclinations (Wake et al. 2017). All results in Sections 3 and 4 use weighted mean dot products and bootstrap resampling to compute the standard error of the weighted means.

The MaNGA sample is complete to $\log(M_\star/M_\odot) = 9.61$ for the Secondary sample and $\log(M_\star/M_\odot) = 9.10$ for the Primary sample (Wake et al. 2017); thus, we require $\log(M_\star/M_\odot) > 9.6$ for comparison to mass-dependent alignment in simulations (Section 4), limiting this comparison to 2551 galaxies. Additionally, the Secondary sample is incomplete for highly inclined galaxies slightly above $\log(M_\star/M_\odot) = 9.61$ (Wake et al. 2017), although such galaxies only constitute a small portion of the sample in the lowest mass bin.

Gross galaxy properties such as absolute magnitude, color, stellar mass, and photometric shape are extracted from the MaNGA targeting catalog, v1_0_1 of the NASA-Sloan Atlas

(Blanton et al. 2011). This catalog is superior to the SDSS catalog for photometry of bright extended galaxies. We use magnitudes and stellar masses from elliptical Petrosian photometry, recommended as the most reliable photometry in the catalog.[13] We use the Sérsic photometry for axis ratios and photometric position angles. The stellar masses and star formation rates are calculated using the K-CORRECT code (Blanton et al. 2003) with a Chabrier (2003) initial mass function. In Figure 2, we show the redshift and mass distribution of the final sample of 2736 galaxies.

We use Galaxy Zoo for morphological classification (Lintott et al. 2011), matching each MaNGA galaxy to the nearest Galaxy Zoo source within 0.″5. The Galaxy Zoo catalog gives a probability that each galaxy is a spiral (clockwise or counter-clockwise), elliptical, edge-on, merger or unknown morphology. To study the morphological dependence of spin-filament alignments, we only use galaxies with a >50% probability of any single classification. Edge-on galaxies are defined as galaxies with axis ratio $r < 0.3$ rather than using Galaxy Zoo, as Galaxy Zoo classifies any galaxy with spiral structure as a spiral even if it is nearly edge-on. Our final sample therefore contains 1039 elliptical galaxies, 676 spiral galaxies, and 344 edge-on galaxies, with the rest unclassified.

We use the stellar velocity maps produced by the Data Analysis Pipeline (DAP) for MPL-6 (Westfall et al. 2019), which uses the penalized-pixel fitting method (pPXF; Cappellari & Emsellem 2004) to determine kinematic parameters. For the spectrum in each spaxel, the DAP first fits the stellar continuum using the MILES stellar library (Sánchez-Blázquez et al. 2006) and masking emission lines. Emission lines are subsequently fit, fixing the stellar continuum to the previously determined best-fit values.

To check the robustness of our results, we measure galaxy spins from both the stellar continuum and the Hα emission line velocity maps. We apply the same fitting methods (Section 2.3) to both velocity maps. These measurements trace different physical components of the galaxy: the stellar continuum traces the stars and the emission line traces the gas.

2.3. Galaxy Spins

We determine the spin vector for each galaxy by measuring the kinematic position angle using integral-field data from the MaNGA survey. Specifically, the plane-of-sky projection of the spin vector is perpendicular to the kinematic position angle (Figure 3). For each galaxy we determine a single global position angle (and thus spin direction) from the full data cube. We apply the FIT_KINEMATIC_PA routine (Krajnović et al. 2006) to determine the kinematic position angle for each galaxy from the stellar velocity maps, using velocities from the unbinned spaxels (see Appendix A for further details). Our method is necessarily 2D, consistent with our 2D filament finder. In accordance with the 2D nature of our measurement, we hereafter refer to the plane-of-sky projection of the spin as the galaxy spin vector. While the 3D spin could be estimated using the galaxy's axis ratio to find the inclination (Haynes & Giovanelli 1984), this method requires an estimate of the galaxy's intrinsic thickness; assumes that the galaxy's shape can be approximated by an oblate spheroid, which may not be valid for elliptical galaxies; and could be biased by the isophote used or the presence of a galactic bulge (Andrae & Jahnke 2011; Kirk et al. 2015). Moreover, estimating the 3D spin from the galaxy's shape necessarily leads to anisotropic errors between the plane of sky and the line of sight and potentially an inhomogeneous distribution of inclinations (e.g., Tempel et al. 2013; Tempel & Libeskind 2013).

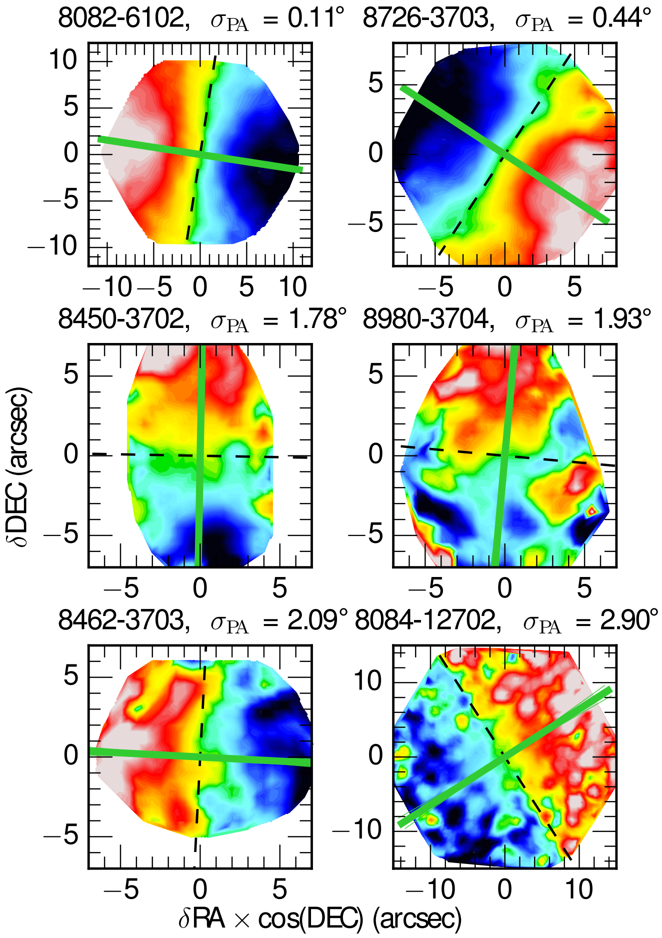

Figure 3. Six randomly selected galaxies with stellar velocity maps and FIT_KINEMATIC_PA fits. The best-fit kinematic position angle is the thick green line and the spin vector is the dashed black line. The thin green lines (often obscured by the thick green line) show the 1σ uncertainty on the position angle. The title gives the plate and IFU ID uniquely identifying each observation and the error on the PA in degrees.

We show six randomly selected fits in Figure 3. The output of FIT_KINEMATIC_PA agrees well with the position angle one would identify by eye. However, FIT_KINEMATIC_PA fails in cases where there are multiple kinematically distinct galaxies in the IFU. In these cases, FIT_KINEMATIC_PA spuriously identifies the line connecting the galaxies as the position angle (Figure 4). We identify these cases by searching for galaxies with multiple SDSS $r < 20$ sources located within the IFU and visually inspect each image to distinguish contaminants from foreground stars, background galaxies, and errors in SDSS photometry. We find and exclude 171 galaxies with spurious fits due to multiple kinematically distinct galaxies in the IFU.

Visual inspection shows that the velocity maps become increasingly noisy, with poorly defined rotation, when $\sigma_{PA} > 5°$. As a result, we remove these 858 galaxies from our measurement. Using a stricter cut of $\sigma_{PA} < 3°$ changes the results presented in Table 1 by $\lesssim 1\sigma$.

In the bottom panel of Figure 1, we plot galaxy spin vectors and filaments for a small region of the sky at $z = 0.025$–0.03 to

---

[13] See http://www.sdss.org/dr13/manga/manga-target-selection/nsa/.

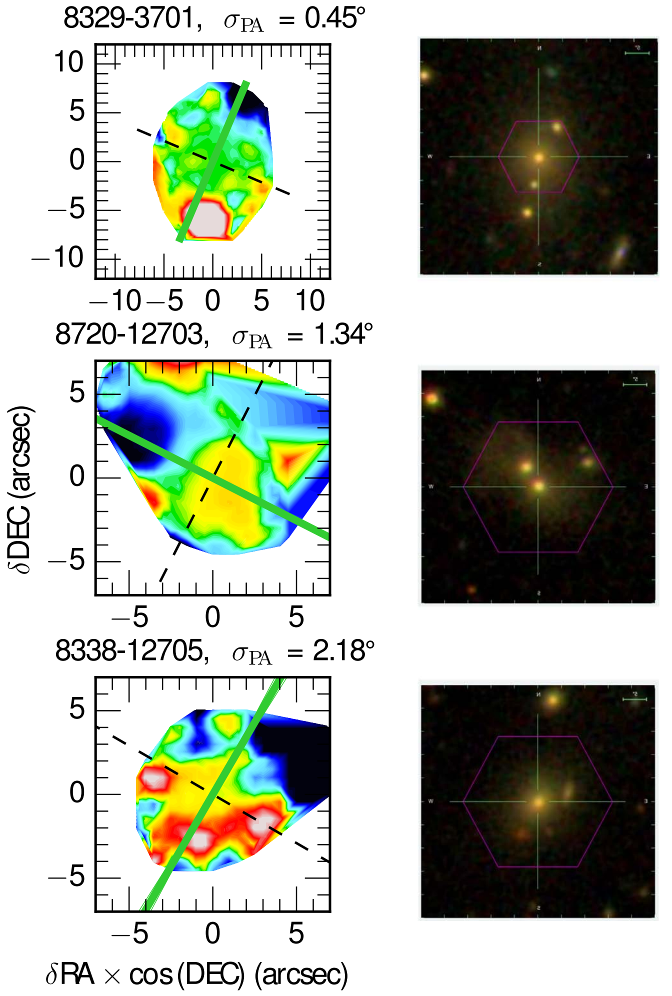

Figure 4. Three randomly selected cases with multiple galaxies inside the IFU. Panels on the left show the stellar velocity maps and FIT_KINEMATIC_PA fits. Panels on the right show the SDSS image with the MaNGA IFU overlaid. Although the fitting errors on these galaxies are formally smaller than the cutoff for poorly measured spins (error $> 5°$), it is clear from comparison to the SDSS images that the fit is spurious due to multiple galaxies in the IFU.

illustrate the alignment measurement. We are searching for a weak alignment identifiable statistically but not visually.

In Figure 5, we show that the measurement errors on the filaments (blue) dominate the errors on the galaxy position angles (red). We also plot the distribution of stellar minus emission line position angle; because this dispersion is the quadrature sum of the measurement error on the position angle and the true dispersion between the stellar and emission line spins, it provides an upper bound on the position angle error. This dispersion is still smaller than the filament error, showing that the filament error must be greater than the position angle error.

2.4. Mock Spins and Filament Catalogs from Hydrodynamical Simulations

We compare our results to galaxy alignments measured in two publicly available cosmological hydrodynamical simulations, MassiveBlack-II (Khandai et al. 2015) and Illustris-1[14] (Vogelsberger et al. 2014; Nelson et al. 2015). Because the spin-filament alignment signal is quite subtle, we require large box hydrodynamical simulations ($L \gtrsim 100$ Mpc).

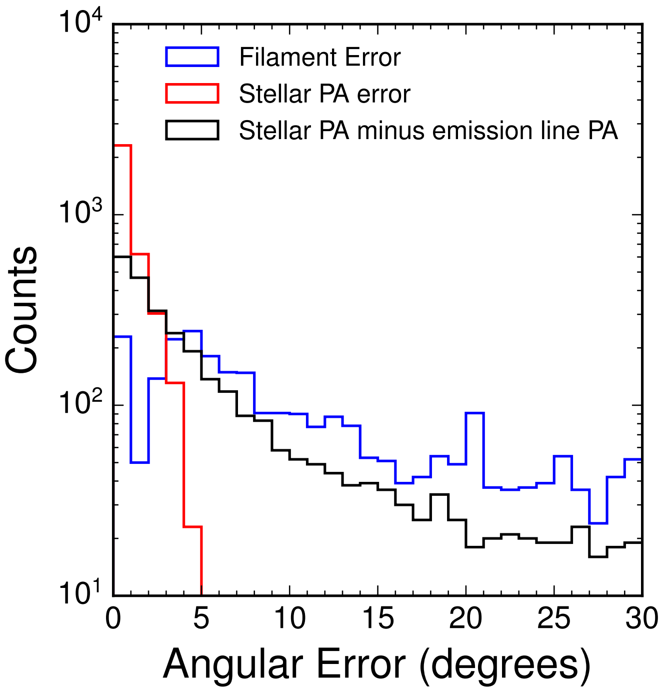

Figure 5. Comparison between the error on the filament angle nearest to each galaxy (blue), the error on the stellar position angle (red), and the dispersion between the stellar position angle and the emission line position angle (black).

MassiveBlack-II is a cosmological simulation run using the smoothed particle hydrodynamics code *GADGET* in a $100\,h^{-1}$ Mpc box with $\Omega_m = 0.275$, $h = 0.704$, and $\sigma_8 = 0.816$ (Khandai et al. 2015). The simulation contains 2×1792^3 particles, with a dark matter particle mass of $1.1 \times 10^7\,h^{-1}\ M_\odot$ and gas particle mass $2.2 \times 10^6\,h^{-1}\ M_\odot$. MassiveBlack-II includes subgrid models for star formation and black hole feedback. Star formation occurs according to the multiphase model of Springel & Hernquist (2003), and young stars and supernovae provide feedback by heating the diffuse ISM. Gas is accreted onto black holes following Bondi accretion, limited to twice the Eddington accretion rate, and 5% of the energy radiated by the accreting black hole is deposited as feedback. Halos are identified using a friends-of-friends algorithm with linking length $b = 0.2$, and subhalos are identified using SUBFIND. Halos and subhalos are required to have at least 40 dark matter and gas particles; therefore, the stellar mass limit of the simulation is $1.26 \times 10^8 M_\odot$.

In MassiveBlack-II, the spin for each galaxy is defined as the unit stellar angular momentum vector. Galaxy spins are only computed for subhalos with at least 1000 dark matter and star particles. This corresponds to a stellar mass limit of $\log(M_\star/M_\odot) = 9.5$ for the sample with measured spins; thus the spin subsample is complete for the mass range of the MaNGA sample ($\log(M_\star/M_\odot) > 9.6$), confirming the validity of comparing data to simulations over this mass range. We also consider alignments between filaments and gas spins in MassiveBlack-II, where gas spins are computed for subhalos with at least 1000 gas particles.

Illustris-1 is run using the moving-mesh code AREPO in a $75\,h^{-1}$ Mpc box with 1820^3 gas and dark matter particles each for a dark matter particle mass of $6.3 \times 10^6 M_\odot$ and a gas particle mass of $1.3 \times 10^6 M_\odot$. Subhalos are required to have at

---

[14] http://www.illustris-project.org/data/

least 20 particles[15]; therefore, the stellar mass limit is $2.6 \times 10^7 M_\odot$. The cosmological parameters are $\Omega_m = 0.2726$, $h = 0.704$, and $\sigma_8 = 0.809$. The subgrid physics is described extensively in Vogelsberger et al. (2013) and is similar to the subgrid physics in MassiveBlack-II, but somewhat more elaborate: Illustris-1 uses variable wind speeds and mass loading in the Springel & Hernquist (2003) galactic wind model, and Illustris-1 includes radio-mode active galactic nucleus (AGN) feedback as well as quasar-mode feedback.

Halos in Illustris-1 are identified using a friends-of-friends algorithm with linking length $b = 0.2$ on the dark matter particles, and subhalos are subsequently identified using SUBFIND. For both MassiveBlack-II and Illustris, the masses quoted in this paper (both dark matter and stellar) are defined as the total mass of all particles bound to a given SUBFIND halo. As in MassiveBlack-II, subhalo spin is defined as the unit stellar angular momentum vector (Zjupa & Springel 2017), summing over all star particles within twice the stellar half-mass–radius.

Angular momenta are only calculated for subhalos with more than 300 dark matter particles, yielding a stellar mass limit of $3.8 \times 10^8 M_\odot$ for halos with the cosmic baryon fraction. Therefore, as for MassiveBlack-II, it is valid to compare simulation and data alignments for MaNGA galaxies with $\log(M_\star/M_\odot) > 9.6$.

Since we measure filaments using Cosmic Web Reconstruction in two dimensions, some filaments in our catalogs may just be cuts through sheets lying perpendicular to the plane of the sky. Since halo alignments with sheets may be different from halo alignments with filaments (e.g., Aragón-Calvo et al. 2007b, find a mass-dependent transition from alignment to anti-alignment with filaments, but mass-independent alignment between halos and sheets), our alignment measurements are not directly comparable to 3D filament alignment measurements in simulations. Therefore, we compare our measurement to mock observations in MassiveBlack-II and Illustris-1 reproducing the 2D filaments used in the observational work.

For both Illustris-I and MassiveBlack-II, we create a mock filament catalog for each of the 26 Cosmic Web Reconstruction $\Delta z = 0.005$ slices between $z = 0.02$ and $z = 0.15$. These 26 filament catalogs allow us to create a mock galaxy-filament alignment measurement by matching the redshift distribution of the MaNGA galaxies. For each redshift slice, we select subhalos in descending order of mass to match the number density of SDSS galaxies in that redshift slice. We define filaments using subhalos rather than halos or dark matter particles because subhalos are generally taken as proxies for galaxies in, e.g., comparisons to the galaxy stellar mass function (Vogelsberger et al. 2014; Khandai et al. 2015). Since the completeness of the SDSS Main Galaxy Sample is >90% (Strauss et al. 2002), this procedure yields a mock sample representative of MGS. We move the subhalos into redshift space and divide the box into seven slices along the z axis (width $14\,h^{-1}\,\mathrm{Mpc} = 20$ Mpc), finding filaments in two dimensions in each slice following the same method as in the data. We generate the smoothed density field from subhalos in the 90% densest environments, match the smoothing bandwidth at each redshift to the bandwidth used in the data, and identify the filament direction using local PCA. We ignore the periodic boundary conditions of the box when finding filaments. With these 26 filament catalogs we can then make a mock observation of galaxy-filament alignment by randomly assigning each galaxy in the simulation to one of the 26 catalogs following the redshift distribution of the data (see Section 4 for further details).

3. Galaxy-filament Alignments of Entire Sample

After the quality cuts described above and the redshift cut ($0.02 < z < 0.15$), we measure alignments with a sample of 2736 galaxies. We measure alignment using the mean dot product between the unit filament vectors and the unit galaxy spin vectors. A dot product of 1 indicates perfect alignment, 0 indicates perfect anti-alignment, and $2/\pi = 0.6366$ (i.e., the average value of $\cos\theta$ over the range 0–π) indicates random alignment. All mean dot products are defined as weighted means using the MaNGA weights defined to recover a volume-limited sample (Wake et al. 2017). Error bars are defined for the weighted means using 50,000 bootstrap resamples of each galaxy subsample. We compare the measured alignment to a random signal generated from 50,000 shuffles of the galaxy and filament catalogs; if there are anisotropies in the galaxy and filament catalogs, the expectation for random alignments will deviate from $2/\pi$. In fact, deviations from $2/\pi$ are modest for all subsamples.

We find no evidence for alignments between galaxy spins and filaments, with a mean dot product of 0.6452 ± 0.0075, and 0.61σ deviation from the shuffled dot product of 0.6406.

In Table 1, we split the sample in several ways: four equal-sized groups of distance to the nearest filament D_F, stellar mass, and $u - r$ color; and spiral, elliptical, and edge-on galaxies. We do not find significant alignments for any of the groups, nor do we find significant linear trends with any of these properties.

We also measure alignments with the Bisous model filaments of Tempel et al. (2014), and find similar results (Table 2). While the overall alignments are stronger for the Bisous filaments (1.16σ versus 0.61σ), in neither case are they statistically significant, and we do not find statistically significant alignments with any subsample in mass, color, distance to filament, or morphological type for the Tempel et al. (2014) filaments. The similar alignment results with the two filament finders, despite the drastic methodological differences between the Bisous model and the Cosmic Web Reconstruction filaments, bolster our conclusion that the MaNGA galaxies lack significant alignments with filaments.

Figure 6 shows that the distribution of $\cos\theta$ is fully consistent with random alignments. The scatter in $\cos\theta$ is dominated by intrinsic scatter in the alignments between galaxy spins and filaments, rather than measurement error from either the galaxy spins or the filament directions. By measuring the total scatter in the galaxy-filament alignments and subtracting the contribution from measurement error in quadrature, we can estimate the intrinsic scatter in alignments between galaxy spins and filaments. We estimate the contribution from measurement error by creating 50,000 realizations of the alignment data set in which each filament or position angle is drawn from a Gaussian with standard deviation given by the reported measurement error. We find that the standard deviation of the resulting mean dot product (i.e., the scatter from measurement error) is 0.0044. The total standard error of 0.0075 is slightly higher than the standard error expected if the galaxies and filaments were entirely randomly aligned, 0.0074. Since the standard error cannot extend higher than ~0.0074, at

---

[15] http://www.illustris-project.org/data/docs/faq/#cat3

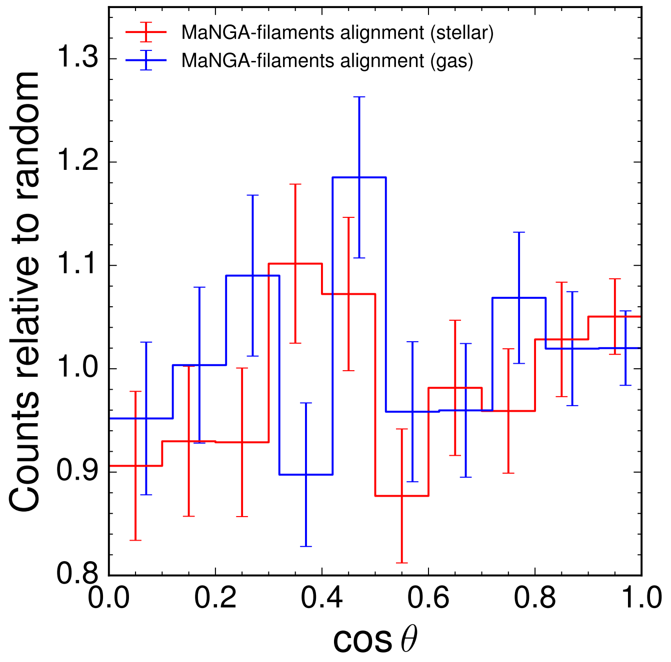

Figure 6. Distribution of $\cos\theta$ (angle between galaxy spin and Cosmic Web Reconstruction filament direction; red for stellar spins and blue for emission line spins) compared to random alignments. Each histogram is divided by the expectation for random alignments in that bin. Error bars are computed from Poisson statistics and the gas-filament alignment histogram is offset for clarity.

this point the quadrature sum of the intrinsic scatter and measurement error may exceed the total scatter, and thus we can only place a lower bound on the intrinsic scatter, $\sigma_i \geqslant 0.0061$.

4. Mass Dependence of Spin-filament Alignments

4.1. Comparison to Mass-dependent Alignments in Simulations

Previous work has found that galaxy spin-filament alignments in *N*-body and hydrodynamical simulations are mass-dependent, with lower-mass galaxies showing alignment and higher-mass galaxies showing anti-alignment (Bailin & Steinmetz 2005; Aragón-Calvo et al. 2007b; Hahn et al. 2007; Codis et al. 2012, 2015; Trowland et al. 2013; Aragon-Calvo & Yang 2014; Dubois et al. 2014). As a result of this mass dependence, it is possible that a significant alignment signal could be concealed by opposing contributions from high- and low-mass galaxies. Therefore, we study the mass dependence of the alignment signal and compare it to mass-dependent alignments in the MassiveBlack-II and Illustris-1 simulations. We attempt to mimic the construction of the spin and filament catalogs as closely as possible to present a fair and quantitative comparison between data and simulations.

We separate galaxies in the data and simulations into five bins of $\Delta\log M_\star = 0.5$, with the lower limits of each bin ranging from $10^{9.6}\ M_\odot$ to $10^{11} M_\odot$ (the lowest bin has $\Delta\log M_\star = 0.4$). We ignore galaxies less massive than $10^{9.6}\ M_\odot$ because MaNGA is incomplete below this mass, yielding a sample of 2551 MaNGA galaxies. While the individual stellar masses have relatively large uncertainties (0.2–0.3 decades; Blanton & Roweis 2007; Conroy 2013), each bin in stellar mass has >100 galaxies, thus the mass uncertainties are much smaller than the bin sizes.

Table 2
Bisous Filament Alignments for Different Subsamples

Sample	N	$\langle\cos\theta\rangle$	SE	Shuffle Mean	σ from Shuffle
All	2546	0.6462	0.0079	0.6370	1.16
$D_F < 0.3$ Mpc	635	0.6265	0.0178	0.6357	−0.57
$0.3 < D_F < 1.0$ Mpc	637	0.6360	0.0151	0.6375	−0.04
$1.0 < D_F < 1.8$ Mpc	636	0.6493	0.0152	0.6402	0.83
$D_F > 1.8$ Mpc	638	0.6716	0.0150	0.6363	2.32
$M_\star < 9.89$	636	0.6377	0.0137	0.6369	0.08
$9.89 < M_\star < 10.38$	637	0.6619	0.0123	0.6371	2.05
$10.38 < M_\star < 10.82$	636	0.6487	0.0130	0.6388	0.94
$M_\star > 10.82$	637	0.6259	0.0160	0.6363	−0.67
$u - r < 1.65$	636	0.6369	0.0151	0.6367	0.02
$1.65 < u - r < 2.06$	637	0.6679	0.0146	0.6370	2.15
$2.06 < u - r < 2.33$	636	0.6343	0.0142	0.6393	−0.16
$u - r > 2.33$	637	0.6498	0.0159	0.6343	0.83
elliptical	1030	0.6489	0.0122	0.6368	1.01
spiral	667	0.6558	0.0147	0.6361	1.30
edge-on	338	0.6262	0.0211	0.6396	−0.50

Note. MaNGA spin-Bisous filament alignments for the entire sample and subsamples split by distance to filament (D_F), stellar mass (in units of $\log M_\odot$), $u - r$ color, and morphology. $\langle\cos\theta\rangle$ is the mean dot product between the unit spin vector and the unit filament vector. SE is the standard error of the mean, calculated using 50,000 bootstrap resamples of the data. We measure the expectation for random alignments using 50,000 shuffles of the data, and compute σ, the deviation between the data and the randoms in units of the standard error.

The redshift distribution of each stellar mass bin is quite different due to the strong correlation between redshift and stellar mass in the MaNGA sample (Figure 2). Furthermore, the number density of galaxies in the SDSS Main Galaxy Sample is a strong function of redshift, thus the fidelity of recovery of the filaments will be better at low redshift than at high redshift. These effects may introduce a spurious mass dependence into the alignment signal. The hydrodynamical simulation boxes are only $100\,h^{-1}$ Mpc, so we cannot create a lightcone mocking the SDSS Main Galaxy Sample. Instead, we create 26 different realizations of the filament catalogs with filaments found using different subhalo densities (i.e., representing different galaxy densities), corresponding to the redshift slices of the filament catalog, as described in Section 2.4. In each realization, we find filaments in two dimensions as in the data. We assign each galaxy to one of the 26 different filament catalogs by drawing from the redshift distribution of the MaNGA galaxies at a given mass, weighted by the MaNGA volume weights. In this way, we assign each galaxy in the simulation to a unique filament, and measure the 2D spin-filament alignment in the same manner as in the data. We estimate error bars using the standard error of the mean of each bin, and average over 100 random draws from the mass-redshift distribution. We assess the discrepancy between data and simulation using χ^2, with errors given by the quadrature sum of the error bars on the data and error bars on the simulation.

This methodology yields different spin-filament alignments from the standard picture, with weak anti-alignments seen at all masses, rather than a transition from alignments at low mass to anti-alignments at high mass. This discrepancy arises from the enforced degeneracy between mass and redshift: at high mass the sample is dominated by high-redshift galaxies, which are associated with more poorly measured filaments due to the

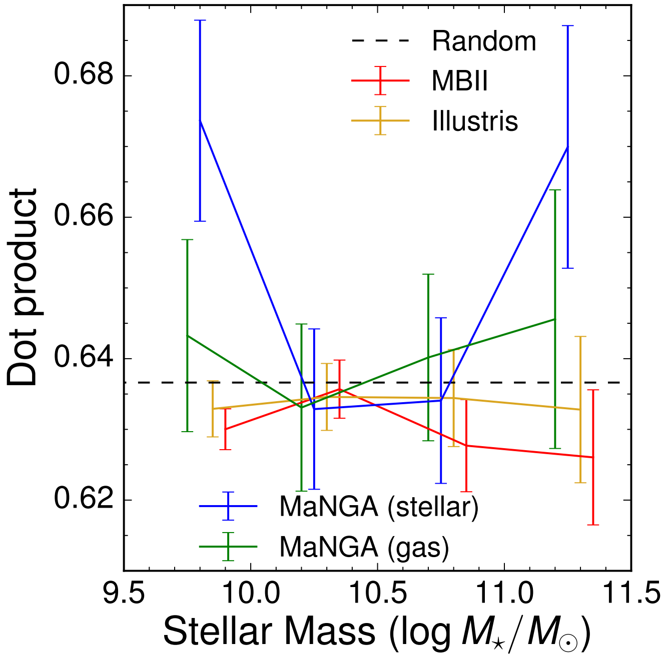

Figure 7. Mass dependence of MaNGA spin-filament alignment, comparing MaNGA alignments using both stellar (blue) and emission line (green) spins to alignments in the MassiveBlack-II (red) and Illustris (orange) simulations. In each bin, points from different samples are offset for clarity.

lower number density in the Main Galaxy Sample at higher redshift. While high-mass galaxies show stronger anti-alignments than low-mass galaxies at fixed redshift, the strong anti-alignment at high masses is weakened by the degeneracy between mass and redshift. The difference between the simulation curves in Figure 7 and the standard picture highlights the importance of constructing a simulation sample that closely mimics the methodology of the data.

For the fiducial case, we find modest tension between the mass dependence of alignments in the MaNGA sample of 2551 galaxies and the mass dependence in the hydrodynamical simulations, with $\chi^2 = 14.26$ over 4 degrees of freedom ($p = 0.0065$, equivalent to 2.7σ) for MassiveBlack-II and $\chi^2 = 11.09/4$ dof ($p = 0.026$, equivalent to 2.2σ) for Illustris. We find similar 2σ–3σ tensions when using different bins, and in fact find a higher $\chi^2 = 15.52$ when using a stricter cut of $\sigma_{\rm PA} < 3°$, indicating that the tension is not an artifact of the binning scheme and cuts used. However, this tension is clearly absent in the mass dependence of alignments for Hα emission line spins, for which we find $\chi^2 = 2.59$ over 4 degrees of freedom between the data and MassiveBlack-II.

We confirm that the χ^2 test is appropriate for this comparison: the mean dot product in each stellar mass bin is normally distributed, and the covariance between neighboring bins is small compared to the variance of each bin. Using 50,000 bootstrap resamples, we confirm that the distribution of the mean dot product in each mass bin is normally distributed, even in cases where there are only ~50 galaxies in the smallest (most massive) bin. We estimate the covariance by resampling the galaxies in 100 deg^2 blocks rather than resampling galaxy by galaxy in order to preserve the source of the covariance, correlations between neighboring galaxy spin-filament dot products arising from galaxy spin correlations, which drop rapidly over $\sim 10\,h^{-1}$ Mpc (Pen et al. 2000; Lee 2011). We find that computing the χ^2 with this covariance matrix rather than assuming a diagonal covariance matrix makes little difference, and that the resulting covariance matrices are relatively robust to changes in the size of the resampling blocks. Given that MaNGA galaxies are widely distributed over the sky, with the average pair separation greater than the $\sim 10\,h^{-1}$ Mpc spin correlation length (Figure 1), we expect the covariance matrix to be nearly diagonal.

Table 3
MaNGA Spin Measurement Completeness

Bin	Stellar Completeness	Emission Line Completeness
$9.6 < \log h^{-1}M_\odot < 10$	83.7%	91.3%
$10 < \log h^{-1}M_\odot < 10.5$	97.1%	91.3%
$10.5 < \log h^{-1}M_\odot < 11$	95.6%	90.0%
$\log h^{-1}M_\odot > 11$	76.2%	76.2%

Note. Fraction of MaNGA galaxies with well-measured spins (error <5°) in different mass bins.

The sample of MaNGA galaxies with well-measured spins is not complete: in fact, the completeness varies as a function of mass, with low- and high-mass galaxies having relatively low completeness of well-measured stellar spins, whereas intermediate-mass galaxies are quite complete (Table 3). This incompleteness preferentially selects galaxies with higher specific angular momentum j, for which it is easier to measure a spin direction. This could possibly bias the mass dependence of spin-filament alignments, if high j galaxies have different alignments than low j galaxies. We attempt to estimate the bias introduced by this incompleteness by removing low j subhalos in the mass bins in the simulation to match the incompleteness of stellar spins in MaNGA. This is a conservative procedure, as incompleteness is likely also caused by low-S/N stellar continuum and plane-of-sky inclinations, which are not related to galaxy-filament alignment strength. Nevertheless, removing low-j subhalos has an extremely modest effect on alignments in the simulations, changing the χ^2 between data and Illustris from 11.09 to 12.57.

These tests suggest that the comparison between data and simulations presented above is not impacted by covariance between the stellar mass bins or incompleteness in the spin measurements. Therefore, the discrepancy between the spin-filament alignments in the data and simulations remains unresolved.

4.2. 3D Alignments in Simulations

While the mass-dependent alignment signal in the data is quite modest, more significant differences become apparent if we instead use simulated filaments with no regard to observational constraints, i.e., filaments in three dimensions and filaments measured using all subhalos, rather than only using massive observable galaxies. This allows us to detect galaxy-filament alignments at much higher significance.

Both MassiveBlack-II and Illustris show similar mass dependence of the alignments between dark matter spins and filaments (Figure 8). This transition from being aligned at low masses to being anti-aligned at higher masses is consistent with previous findings, mostly from dark-matter-only simulations (Bailin & Steinmetz 2005; Aragón-Calvo et al. 2007b; Hahn et al. 2007; Pichon et al. 2011; Codis et al. 2012, 2015;

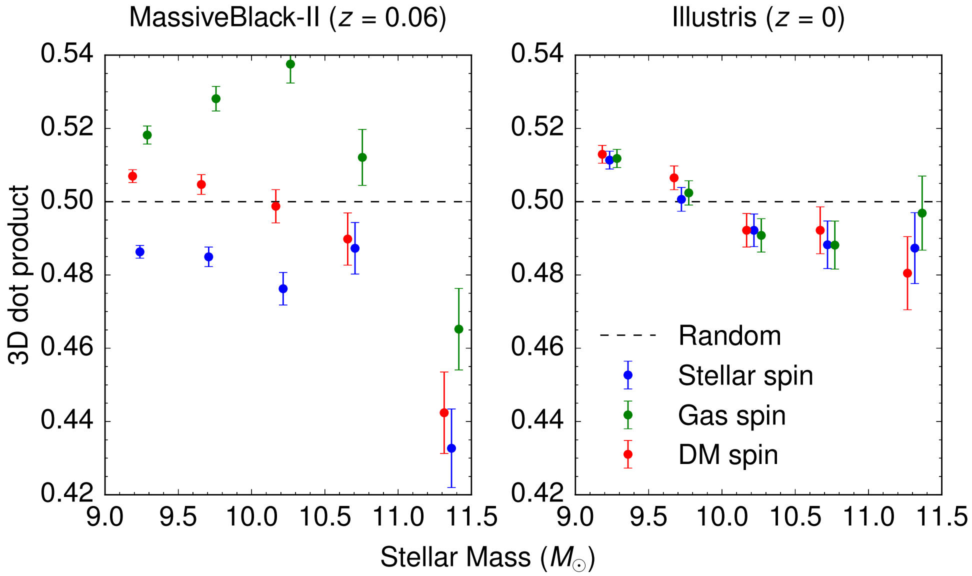

Figure 8. 3D alignments between subhalo spins and "ideal" filaments measured using the 500,000 most massive subhalos in Illustris ($z = 0$) and MassiveBlack-II ($z = 0.06$). In both panels, the black dotted line is the 3D dot product expected for random alignments, the red (blue; green) points are alignments between dark matter (stellar; gas) spins and filaments. Points are offset in mass for clarity.

Trowland et al. 2013; Aragon-Calvo & Yang 2014; Dubois et al. 2014).

In contrast, Illustris and MassiveBlack-II paint opposing pictures of the mass dependence of stellar spin-filament alignments. In Illustris the mass dependence of the stellar spin alignments is quite similar to the mass dependence of the dark matter spin alignments, while in MassiveBlack-II the stellar spin alignments show a qualitatively different behavior than the dark matter spin alignments, remaining anti-aligned even at the lowest masses (Figure 8). The $z \sim 0$ results in Illustris are consistent with the findings of Dubois et al. (2014) in the Horizon-AGN hydrodynamic simulation at $z = 1.8$, who measured alignments between filaments and stellar angular momentum and found a transition from alignment to anti-alignment at $M_\star \sim 10^{10.5}\ M_\odot$.

The mass-dependent trends in gas spin alignments are even more divergent between Illustris and MassiveBlack-II. Gas-filament alignments in Illustris are quite similar to star-filament and dark matter-filament alignments, but gas spins in MassiveBlack-II remain aligned with filaments until $M_\star \sim 10^{11}\ M_\odot$, and the alignments are considerably stronger than low-mass dark matter-filament alignments. While gas spins in MassiveBlack-II are only measured for a subset of galaxies with >1000 gas particles, this subset has very similar stellar-filament and dark matter-filament alignments as the entire sample, implying that the gas-filament alignments are not significantly impacted by selection bias.

Taken together, these results suggest that while the "transition-mass" picture presented in previous work (e.g., Codis et al. 2012) remains valid for dark matter spins, its validity for stellar and gas spins of galaxies is questionable and apparently dependent on subgrid physics and feedback models.

In conclusion, we find modest tension between the mass dependence of galaxy-filament alignments in MaNGA and in the MassiveBlack-II and Illustris simulations. The tension is present if MaNGA spins are estimated using stellar continuum velocities, although it disappears if we use MaNGA spins measured from the Hα emission line. While we find minimal differences in alignments between MassiveBlack-II and Illustris using a sample of simulated galaxies and filaments selected to mimic the MaNGA and SDSS galaxy samples, an ideal measurement using filaments constructed from all subhalos in the simulations reveals a significant difference in the behavior of spin alignments in Illustris and MassiveBlack-II at low masses. While both simulations find that dark matter spins are aligned with filaments at low mass, in agreement with previous results from N-body simulations, Illustris finds stellar spin-filament alignment at low mass, while MassiveBlack-II finds stellar spin-filament anti-alignment.

5. Discussion

We present the first measurement of alignments between filaments and galaxy spins as measured from integral-field kinematics. We find no significant detection of galaxy spin alignments with filaments. We find that the mass dependences of spin-filament alignments from MaNGA are in 2σ–3σ tension with spin-filament alignments from the MassiveBlack-II and Illustris simulations, although the tension disappears if we instead use galaxy spins measured from the Hα emission line. While the predictions of MassiveBlack-II and Illustris are essentially identical if we use a "mock-observational" sample, 3D filaments measured using all subhalos in the simulation reveal significant differences in alignment behavior at low masses, suggesting that the "transition-mass" picture described in previous works is dependent on the feedback and subgrid physics.

Previous studies have measured galaxy spin-filament alignments using galaxy shape as a proxy for galaxy spin (Tempel et al. 2013; Tempel & Libeskind 2013; Pahwa et al. 2016; Chen et al. 2019). These studies found a weak dichotomy between spiral and elliptical galaxies, with spirals aligned and ellipticals anti-aligned with filaments. We do not find evidence for this dichotomy, but our error bars are larger than those in previous studies and our results are consistent with them.

The results in this work are limited by the relatively small sample size of ~2600 MaNGA galaxies with well-measured spins and sufficient proximity to "Cosmic Web Reconstruction" filaments. The error bars on this measurement are dominated by intrinsic scatter rather than measurement error on the spins or the filaments, suggesting that acquiring larger samples of galaxy spins is the most effective way to achieve a more precise measurement. The full MaNGA sample will provide integral-field-unit spectroscopy for 10,000 galaxies, roughly doubling the sample with sufficient spin measurements. This represents a significant step forward, but even larger samples are needed to distinguish the alignment models of different simulations at high significance. The proposed Hector survey on the Anglo-Australian Telescope could deliver integral-field spectroscopy for up to 100,000 galaxies over the next decade (Bryant et al. 2016), offering an unparalleled ability to learn about the relationship between galaxy spin and large-scale structure and the acquisition of galaxies' angular momentum.

We thank Simone Ferraro, Joanne Cohn, and Shy Genel for helpful comments and discussions.

This research made use of Marvin, a core Python package and web framework for MaNGA data, developed by Brian Cherinka, José Sánchez-Gallego, Brett Andrews, and Joel Brownstein (Cherinka et al. 2018).

Calculations presented in this paper used resources of the National Energy Research Scientific Computing Center (NERSC), which is supported by the Office of Science of the U.S. Department of Energy under Contract No. DE-AC02-05CH11231.

Funding for the Sloan Digital Sky Survey IV has been provided by the Alfred P. Sloan Foundation, the U.S. Department of Energy Office of Science, and the Participating Institutions. SDSS acknowledges support and resources from the Center for High-Performance Computing at the University of Utah. The SDSS website is www.sdss.org.

SDSS is managed by the Astrophysical Research Consortium for the Participating Institutions of the SDSS Collaboration including the Brazilian Participation Group, the Carnegie Institution for Science, Carnegie Mellon University, the Chilean Participation Group, the French Participation Group, Harvard-Smithsonian Center for Astrophysics, Instituto de Astrofísica de Canarias, The Johns Hopkins University, Kavli Institute for the Physics and Mathematics of the Universe (IPMU)/University of Tokyo, Lawrence Berkeley National Laboratory, Leibniz Institut für Astrophysik Potsdam (AIP), Max-Planck-Institut für Astronomie (MPIA Heidelberg), Max-Planck-Institut für Astrophysik (MPA Garching), Max-Planck-Institut für Extraterrestrische Physik (MPE), National Astronomical Observatories of China, New Mexico State University, New York University, University of Notre Dame, Observatório Nacional/MCTI, The Ohio State University, Pennsylvania State University, Shanghai Astronomical Observatory, United Kingdom Participation Group, Universidad Nacional Autónoma de México, University of Arizona, University of Colorado Boulder, University of Oxford, University of Portsmouth, University of Utah, University of Virginia, University of Washington, University of Wisconsin, Vanderbilt University, and Yale University.

Appendix A
Galaxy Spin Fitting

We use the FIT_KINEMATIC_PA routine (Krajnović et al. 2006) to determine the kinematic position angle for each galaxy from the stellar velocity maps, using velocities from the unbinned spaxels. We remove low-quality or potentially problematic data by masking spaxels with r-band SNR < 5, spaxels with the DONOTUSE or UNRELIABLE bitmasks (Westfall et al. 2019), $|v| > 350\ \mathrm{km\ s^{-1}}$, $\sigma_v > 10^3\ \mathrm{km\ s^{-1}}$, or a velocity that is more than a 5σ outlier (i.e., $|v| > 5$ times the standard deviation of v). We also mask all contiguous regions with SNR > 5 that are disconnected from the central part of the galaxy in order to eliminate faint companion galaxies within the IFU. To avoid giving a large weight to any one spaxel, we set the minimum velocity error to $2\ \mathrm{km\ s^{-1}}$ (Pineda et al. 2017). From visual inspection of the fits, we find that these settings give the best performance. We recenter each galaxy about the unweighted centroid of its unmasked region, because the center of rotation in some galaxies is offset from the center of the IFU. Finally, we perform each fit in curved-sky coordinates ($\alpha \cos \delta$, δ) and convert the resulting position angles to an equirectangular projection for consistency with the filament catalog. We use this method because it fits the position angles in a physical coordinate system.

FIT_KINEMATIC_PA fits a bi-antisymmetric model to a velocity map. For a specified rotation of the xy coordinates relative to the native ($\alpha \cos \delta$, δ) coordinates (i.e., position angle), the bi-antisymmetric model at (x, y) is the average of the velocity at $(\pm x, \pm y)$, linearly interpolating between neighboring points if need be. The best-fit position angle minimizes χ^2 computed from the data, the bi-antisymmetric model, and the MaNGA velocity errors. We initially loop over all PAs between 0° and 180° to ensure that we are near the global minimum, then use Nelder-Mead minimization to find the global minimum χ^2.

To estimate the error on the position angle, we create 100 realizations of the velocity map, drawing the velocity in each spaxel from a Gaussian centered at the measured velocity, with standard deviation equal to the velocity error, and assuming no covariance between neighboring spaxels. We apply the same χ^2 minimization process to each of the 100 realizations, again using the MaNGA velocity errors and the bi-antisymmetric model from FIT_KINEMATIC_PA. We define the position angle as the mean of the ensuing 100 position angles θ_i and the position angle error as the standard deviation of the 100 position angles. We use the circular mean of headless (i.e., spin-2) vectors μ_{180}:

$$\mu_{180}(\boldsymbol{\theta}) = \frac{1}{2} \arctan \frac{\sum \sin 2\theta_i}{\sum \cos 2\theta_i}. \tag{1}$$

The standard deviation is adjusted similarly:

$$\sigma_{180}(\boldsymbol{\theta}) = \sqrt{\frac{1}{N} \sum \min^2(\theta_i - \mu_{180}(\boldsymbol{\theta}),\ 180 - \theta_i + \mu_{180}(\boldsymbol{\theta}))}. \tag{2}$$

While this is only an approximate estimate of the position angle error, and may in particular underestimate the error due to nonzero covariance between neighboring spaxels, the position angle errors are not an important contributor to the total error budget on the alignment measurements: they are dominated by the errors on the filament angles (Figure 5) and as we show in Section 2, the measurement errors are dominated by the intrinsic scatter in galaxy-filament alignments anyway.

Appendix B
3D versus 2D Alignment Measurements in Simulations

We use measurements of galaxy-filament alignments in the MassiveBlack-II simulation to determine how much signal is lost using 2D rather than 3D measurements of the filaments. We generate 3D filaments using the redshift-space positions of the top 500,000 subhalos in MBII by total mass ($\log M_h/M_\odot > 9.74$) and applying the Cosmic Web Reconstruction algorithm with a smoothing bandwidth of 1 h^{-1} Mpc. For the 2D sample, we use the same subhalos and bandwidth, but as in Section 2.4, we split the box into seven slices along the z direction ($\Delta z = 0.005 = 20$ Mpc ~ 14 h^{-1} Mpc) and separately find 2D filaments in each slice. In both cases, the number density of subhalos is much greater than the number density achievable in the Main Galaxy Sample; we use these large samples in order to make a high signal-to-noise measurement of 3D and 2D alignment, and assume that the reduction in signal from three dimensions to two dimensions will be similar for the realistic lower number-density samples.

We find that the mean dot product between the 3D filaments and the subhalo stellar spins is 0.4882 ± 0.00136 compared to an expectation of 0.5 for random alignments for an alignment strength signal-to-noise of 8.68. For the 2D filaments, we find a mean dot product of 0.6293 ± 0.00145 compared to 0.6366 for random alignments, yielding an alignment strength signal-to-noise of 5.03. We also measure alignments between subhalo spins and "ideal" 2D filaments, which are the projection of the 3D filaments onto the xy plane; here, we find a mean dot product of 0.6267 ± 0.00146 and signal-to-noise 6.81. This indicates that most of the reduction in the $\Delta z = 0.005$ case comes from loss of filament information in the z direction and not from the finite Δz of the slices. Therefore, we estimate that using 2D filaments in slices of $\Delta z = 0.005$ reduces the alignment signal strength by 40%. However, it is unlikely that we could realize a 40% improvement in signal using 3D filaments, since the line-of-sight component of the galaxy spin vector is significantly harder to measure than the transverse component, reducing the signal gain from 3D filaments (Krolewski et al. 2017).

ORCID iDs

Alex Krolewski https://orcid.org/0000-0003-2183-7021
Ananth Tenneti https://orcid.org/0000-0003-3933-4756
Dmitry Bizyaev https://orcid.org/0000-0002-3601-133X

References

Alam, S., Albareti, F. D., Allende Prieto, C., et al. 2015, ApJS, 219, 12
Andrae, R., & Jahnke, K. 2011, MNRAS, 418, 2014
Aragón-Calvo, M. A., Jones, B. J. T., van de Weygaert, R., & van der Hulst, J. M. 2007a, A&A, 474, 315
Aragón-Calvo, M. A., van de Weygaert, R., Jones, B. J. T., & van der Hulst, J. M. 2007b, ApJL, 655, L5
Aragon-Calvo, M. A., & Yang, L. F. 2014, MNRAS, 440, L46
Bailin, J., & Steinmetz, M. 2005, ApJ, 627, 647
Bett, P. 2012, MNRAS, 420, 3303
Blanton, M. R., Bershady, M. A., Abolfathi, B., et al. 2017, AJ, 154, 28
Blanton, M. R., Brinkmann, J., Csabai, I., et al. 2003, AJ, 125, 2348
Blanton, M. R., Kazin, E., Muna, D., Weaver, B. A., & Price-Whelan, A. 2011, AJ, 142, 31
Blanton, M. R., & Roweis, S. 2007, AJ, 133, 734
Blanton, M. R., Schlegel, D. J., Strauss, M. A., et al. 2005, AJ, 129, 2562
Blumenthal, G. R., Faber, S. M., Flores, R., & Primack, J. R. 1986, ApJ, 301, 27
Bridle, S., & King, L. 2007, NJPh, 9, 444
Bryant, J. J., Bland-Hawthorn, J., Lawrence, J., et al. 2016, Proc. SPIE, 9908, 99081F
Bullock, J. S., Dekel, A., Kolatt, T. S., et al. 2001, ApJ, 555, 240
Bundy, K., Bershady, M. A., Law, D. R., et al. 2015, ApJ, 798, 7
Cabanela, J. E., & Aldering, G. 1998, AJ, 116, 1094
Cappellari, M., & Emsellem, E. 2004, PASP, 116, 138
Catelan, P., Kamionkowski, M., & Blandford, R. D. 2001, MNRAS, 320, L7
Cautun, M., van de Weygaert, R., Jones, B. J. T., & Frenk, C. S. 2014, MNRAS, 441, 2923
Chabrier, G. 2003, PASP, 115, 763
Chen, Y.-C., Ho, S., Blazek, J., et al. 2019, MNRAS, 485, 2492
Chen, Y.-C., Ho, S., Brinkmann, J., et al. 2016, MNRAS, 461, 3896
Chen, Y.-C., Ho, S., Freeman, P. E., Genovese, C. R., & Wasserman, L. 2015, MNRAS, 454, 1140
Cherinka, B., Andrews, B. H., Sánchez-Gallego, J., et al. 2018, arXiv:1812.03833
Codis, S., Gavazzi, R., Dubois, Y., et al. 2015, MNRAS, 448, 3391
Codis, S., Pichon, C., Devriendt, J., et al. 2012, MNRAS, 427, 3320
Conroy, C. 2013, ARA&A, 51, 393
Danovich, M., Dekel, A., Hahn, O., Ceverino, D., & Primack, J. 2015, MNRAS, 449, 2087
Dekel, A. 1985, ApJ, 298, 461
Doroshkevich, A. G. 1970, Afz, 6, 581
Drory, N., MacDonald, N., Bershady, M. A., et al. 2015, AJ, 149, 77
Dubois, Y., Pichon, C., Welker, C., et al. 2014, MNRAS, 444, 1453
Fall, S. M. 1983, in IAU Symp. 100, Internal Kinematics and Dynamics of Galaxies, ed. E. Athanassoula (Cambridge: Cambridge Univ. Press), 391
Fall, S. M., & Efstathiou, G. 1980, MNRAS, 193, 189
Ganeshaiah Veena, P., Cautun, M., van de Weygaert, R., et al. 2018, MNRAS, 481, 414
Gregory, S. A., Thompson, L. A., & Tifft, W. G. 1981, ApJ, 243, 411
Gunn, J. E., Siegmund, W. A., Mannery, E. J., et al. 2006, AJ, 131, 2332
Hahn, O., Carollo, C. M., Porciani, C., & Dekel, A. 2007, MNRAS, 381, 41
Haynes, M. P., & Giovanelli, R. 1984, AJ, 89, 758
Hirata, C. M., Mandelbaum, R., Ishak, M., et al. 2007, MNRAS, 381, 1197
Hirata, C. M., & Seljak, U. 2004, PhRvD, 70, 63526
Jasche, J., Kitaura, F. S., Li, C., & Enßlin, T. A. 2010, MNRAS, 409, 355
Jones, B. J. T., van de Weygaert, R., & Aragon-Calvo, M. A. 2010, MNRAS, 408, 897
Khandai, N., Di Matteo, T., Croft, R., et al. 2015, MNRAS, 450, 1349
Kirk, D., Brown, M. L., Hoekstra, H., et al. 2015, SSRv, 193, 139
Kirk, D., Rassat, A., Host, O., & Bridle, S. 2012, MNRAS, 424, 1647
Krajnović, D., Cappellari, M., de Zeeuw, P. T., & Copin, Y. 2006, MNRAS, 366, 787
Krolewski, A., Lee, K.-G., Lukić, Z., & White, M. 2017, ApJ, 837, 31
Laureijs, R., Amiaux, J., Arduini, S., et al. 2011, arXiv:1110.3193
Law, D. R., Cherinka, B., Yan, R., et al. 2016, AJ, 152, 83
Law, D. R., Yan, R., Bershady, M. A., et al. 2015, AJ, 150, 19
Lee, J. 2011, ApJ, 732, 99
Lee, J., & Erdogdu, P. 2007, ApJ, 671, 1248
Lee, J., & Pen, U.-L. 2000, ApJL, 532, L5
Lee, J., & Pen, U.-L. 2002, ApJL, 567, L111
Libeskind, N. I., Hoffman, Y., Forero-Romero, J., et al. 2013, MNRAS, 428, 2489
Lintott, C., Schawinski, K., Bamford, S., et al. 2011, MNRAS, 410, 166
LSST Science Collaboration, Abell, P. A., Allison, J., et al. 2009, arXiv:0912.0201
Mandelbaum, R., Blake, C., Bridle, S., et al. 2011, MNRAS, 410, 844
Mo, H. J., Mao, S., & White, S. D. M. 1998, MNRAS, 295, 319
Nelson, D., Pillepich, A., Genel, S., et al. 2015, A&C, 13, 12
Pahwa, I., Libeskind, N. I., Tempel, E., et al. 2016, MNRAS, 457, 695
Peebles, P. J. E. 1969, ApJ, 155, 393
Pen, U.-L., Lee, J., & Seljak, U. 2000, ApJL, 543, L107
Pichon, C., Pogosyan, D., Kimm, T., et al. 2011, MNRAS, 418, 2493
Pineda, J. C. B., Hayward, C. C., Springel, V., & Mendes de Oliveira, C. 2017, MNRAS, 466, 63
Porciani, C., Dekel, A., & Hoffman, Y. 2002, MNRAS, 332, 325
Sánchez-Blázquez, P., Peletier, R. F., Jiménez-Vicente, J., et al. 2006, MNRAS, 371, 703
Slosar, A., Land, K., Bamford, S., et al. 2009, MNRAS, 392, 1225
Smee, S. A., Gunn, J. E., Uomoto, A., et al. 2013, AJ, 146, 32
Sousbie, T., Pichon, C., Colombi, S., Novikov, D., & Pogosyan, D. 2008, MNRAS, 383, 1655
Spergel, D., Gehrels, N., Baltay, C., et al. 2015, arXiv:1503.03757
Springel, V., & Hernquist, L. 2003, MNRAS, 339, 289
Strauss, M. A., Weinberg, D. H., Lupton, R. H., et al. 2002, AJ, 124, 1810

Tempel, E., & Libeskind, N. I. 2013, ApJL, 775, L42
Tempel, E., Stoica, R. S., Martínez, V. J., et al. 2014, MNRAS, 438, 3465
Tempel, E., Stoica, R. S., & Saar, E. 2013, MNRAS, 428, 1827
Trowland, H. E., Lewis, G. F., & Bland-Hawthorn, J. 2013, ApJ, 762, 72
van den Bosch, F. C., Abel, T., Croft, R. A. C., Hernquist, L., & White, S. D. M. 2002, ApJ, 576, 21
Vogelsberger, M., Genel, S., Sijacki, D., et al. 2013, MNRAS, 436, 3031
Vogelsberger, M., Genel, S., Springel, V., et al. 2014, Natur, 509, 177
Wake, D. A., Bundy, K., Diamond-Stanic, A. M., et al. 2017, AJ, 154, 86
Wang, P., Guo, Q., Kang, X., & Libeskind, N. I. 2018, ApJ, 866, 138
Wang, P., & Kang, X. 2018, MNRAS, 473, 1562
Westfall, K. B., Cappellari, M., & Bershady, M. A. 2019, arXiv:1901.00856
White, S. D. M. 1984, ApJ, 286, 38
Yan, R., Bundy, K., Law, D. R., et al. 2016a, AJ, 152, 197
Yan, R., Tremonti, C., Bershady, M. A., et al. 2016b, AJ, 151, 8
Zel'dovich, Y. B. 1970, A&A, 5, 84
Zhang, Y., Yang, X., Wang, H., et al. 2015, ApJ, 798, 17
Zjupa, J., & Springel, V. 2017, MNRAS, 466, 1625